

# **Helical Contour Dynamics**

Tianyi Chu<sup>1\*</sup> and Stefan G. Llewellyn Smith<sup>1,2\*\*</sup>

<sup>1</sup>Department of Mechanical and Aerospace Engineering, Jacobs School of Engineering, UCSD, 9500 Gilman Drive, 92093-0411 La Jolla CA, USA <sup>2</sup>Scripps Institution of Oceanography, UCSD, 9500 Gilman Drive, 92093-0209 La Jolla CA, USA Received June 27, 2021; revised October 06, 2021; accepted October 20, 2021

Abstract—The equations of motion for an incompressible flow with helical symmetry (invariance under combined axial translation and rotation) can be expressed as nonlinear evolution laws for two scalars: vorticity and along-helix velocity. A metric term related to the pitch of the helix enters these equations, which reduce to two-dimensional and axisymmetric dynamics in appropriate limits. We take the vorticity and along-helix velocity component to be piecewise constant. In addition to this vortex patch, a vortex sheet develops when the along-helix velocity is nonzero. We obtain a contour dynamics formulation of the full nonlinear equations of motion, in which the motion of the boundary is computed in a Lagrangian fashion and the velocity field can be expressed as contour integrals, reducing the dimensionality of the computation. We investigate the stability properties of a circular vortex patch along the axis of the helix in the presence of a vortex sheet and along-helix velocity. A linear stability calculation shows that the system is stable when the initial vortex sheet is zero, but can be stable or unstable in the presence of a vortex sheet. Using contour dynamics, we examine the nonlinear evolution of the system, and show that nonlinear effects become important in unstable cases.

MSC2010 numbers: 76B47, 76W05 **DOI:** 10.1134/S1560354721060022

Keywords: vortex dynamics, contour dynamics, vortex patch, vortex sheet, helical geometry

#### 1. INTRODUCTION

Helical tip vortices are commonly found in the wake of rotating bladed devices such as marine propellers, wind turbines and helicopters. They have been the subject of continuing theoretical studies, e.g., the recent papers [8, 24, 30]. Far enough downstream of the rotating device, the flow system is locally helical symmetric, which means that it is locally invariant through a combined translation and rotation about the same axis. This leads to the question of the dynamics of vortices under helical symmetry.

In previous work, [2] studied steady helical vortex structures in a swirl flow both theoretically and numerically; [27] investigated the effect of torsion on the dynamics of a helical vortex filament, while [17] derived an expression for the velocity field in the case of moderate or small pitch. [9] used asymptotic expansions of the Biot – Savart law to obtain the velocity field induced by a helical vortex tube with finite thickness. More recently, [32] found new expressions for the motion of a single helical vortex, and [23] derived closed-form solutions for self-induced motion of helical structures. A parallel line of research has examined the time evolution of helical vortices numerically. Direct numerical simulation (DNS) results for helically symmetric systems were first presented by [4]. This approach was later used to simulate a three-helix vortex system [36] and also the merger of two identical vortices [5]. Subsequently [29] examined the evolution of a single helical vortex at different helical pitch values. The work of [33] proposed a vortex filament approach to describe the interaction

<sup>\*</sup>E-mail: tic173@ucsd.edu

<sup>\*\*</sup>E-mail: sgls@ucsd.edu

of a counter-rotating helical pair based on a Lagrangian description, but helical symmetry is not preserved in the obtained vortex structures.

In this work, we present a contour dynamics method for inviscid vortex patches and sheets with helical symmetry. Contour dynamics is a Lagrangian technique that reduces the evolution of vortex patches to the evolution of their boundaries and thus the dimensionality of the system. Contour dynamics was first proposed by [35] in the case of two-dimensional vortex patches. The reader is referred to [6] and [26] for reviews of this work. Contour dynamics was subsequently used for axisymmetric flows [25, 28, 37]. Further physical effects such as magnetic fields [16], swirl [15, 19] and buoyancy [3] have also been considered. The review [18] summarizes generalizations of contour dynamics with additional physics.

The idea of applying contour dynamics in helical symmetry is mentioned in [26] and reviewed in [18], but a detailed description has not been presented previously in the literature. For helically symmetric flows, [20] found steady vortex structures corresponding to closed contours bounding regions of uniform axial vorticity. It had been pointed out by [7] that material conservation of axial vorticity holds when the velocity component parallel to vortex lines is piecewise constant. We compute velocities by inverting a linear helical operator analytically. In the presence of flow along the helical vortex axis, a vortex sheet develops along the edge of a vortex patch.

Stability is another fundamental dynamic property of vortices. Much work has been carried out to develop theoretical stability analysis of helical vortices. The linear stability of a vortex filament was first studied by [34], who obtained three modes of instability for small displacements. These results were extended by [10], who further explored the stability of multiple helical vortices. Later, [21] proposed a model for the stability of equilibrium helical vortex arrays and [22] generalized the analysis to include vortices embedded in a rotor far wake. The short-wave instability, caused by the curvature of a helical tube, was studied in a series of works [11–14].

We examine the stability of circular vortex patches centered at the origin in helical symmetry. A linear stability analysis is carried out that includes a vortex sheet at the boundary of the patch. The result of [20] of stability in the absence of the sheet is recovered. We then use the contour dynamics method outlined to examine the initial nonlinear evolution of the patch. We do not pursue the integration up to times that would show filamentation or other extreme deformation of the vortices.

In Section 2 we present the governing equations, culminating in two coupled scalar advection equations, reviewing results given previously in, e.g., [20]. In Section 3 we review how to invert the relationship between vorticity and streamfunction using a Green's function approach. In Section 4 we present a formulation of contour dynamics that is, to our knowledge, new. We then examine the stability of circular basic states in Section 5: a general base flow is obtained and its linear stability is analyzed, generalizing previous work. We present contour dynamics results for some of these vortices in Section 6. Finally, conclusions are presented in Section 7, while the Appendices contain some technical calculations.

### 2. HELICALLY SYMMETRIC FLOWS

Consider an inviscid and incompressible flow with helical symmetry [7, 20]. This means that the velocity, vorticity and pressure fields are invariant with respect to the helical vector  $\boldsymbol{h}$ , defined in cylindrical coordinates as

$$\boldsymbol{h} = h^2 (\boldsymbol{e}_z - \epsilon r \boldsymbol{e}_\theta), \tag{2.1}$$

with  $h^2 = (1 + \epsilon^2 r^2)^{-1}$  and  $\epsilon$  the pitch of the helix. Helical symmetry also implies that  $h \cdot \nabla = 0$  for any scalar functions of  $r, \phi$  and t, where  $\phi = \theta + \epsilon z$  is the helical coordinate. When  $\epsilon = 0$ , the flow becomes two-dimensional, while  $\epsilon = \infty$  represents the axisymmetric case. The unit vector for the helical coordinate  $\phi$  is defined by

$$\mathbf{e}_{\phi} = h^{-1}\mathbf{h} \times \mathbf{e}_{r} = h(\mathbf{e}_{\theta} + \epsilon r \mathbf{e}_{z}).$$
 (2.2)

A schematic of the helical coordinate system is shown in Fig. 1. In helical coordinates the gradient operator acting on functions with helical symmetry reduces to  $\nabla = e_r \partial/\partial r + e_{\phi}(rh)^{-1}\partial/\partial \phi$ . Since the velocity and vorticity are divergence-free, we have the following decomposition:

$$\boldsymbol{u} = \boldsymbol{h} \times \boldsymbol{\nabla} \psi + \boldsymbol{h} v, \tag{2.3}$$

$$\boldsymbol{\omega} = \boldsymbol{h} \times \boldsymbol{\nabla} \xi + \boldsymbol{h} \zeta. \tag{2.4}$$

The quantities  $\psi$  and v depend only on r,  $\phi$  and time. From this decomposition, the velocity components in cylindrical coordinates are given by

$$u_r = -\frac{1}{r} \frac{\partial \psi}{\partial \phi}, \qquad u_\theta = h^2 \left( \frac{\partial \psi}{\partial r} - \epsilon r v \right), \qquad u_z = h^2 \left( v + \epsilon r \frac{\partial \psi}{\partial r} \right).$$
 (2.5)

In helical coordinates we obtain

$$u_r = \frac{\mathrm{D}r}{\mathrm{D}t} = -\frac{1}{r}\frac{\partial\psi}{\partial\phi}, \qquad u_\phi = rh\frac{\mathrm{D}\phi}{\mathrm{D}t} = h\frac{\partial\psi}{\partial r}$$
 (2.6)

and  $\mathbf{h} \cdot \mathbf{u} = h^2 v$ .

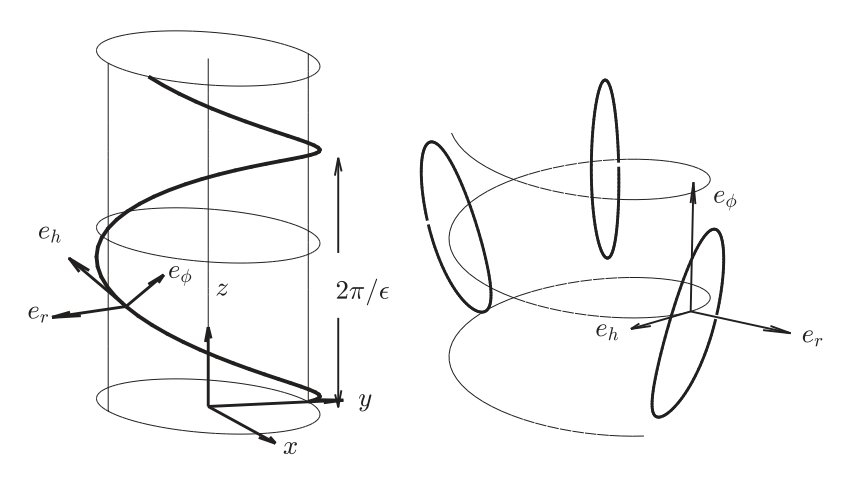


Fig. 1. Schematic of the helical coordinate system (left) and helical contours along the system (right). The axial distance between two turns is  $2\pi/\epsilon$ . Note that the vectors  $\boldsymbol{h}$  and  $\boldsymbol{e}_{\phi}$  lie on the surface of the cylinder r =constant. The special case considered here has the vorticity  $\boldsymbol{\omega}$  everywhere tangent to  $\boldsymbol{h}$ . The contours represent the same patch at different positions along the helical axis.

From the definition of vorticity,  $\omega = \nabla \times u$ , and (2.3)–(2.4), we can show that  $\xi = -v$  and that

$$\mathcal{L}\psi = \frac{1}{r}\frac{\partial}{\partial r}\left(rh^2\frac{\partial\psi}{\partial r}\right) + \frac{1}{r^2}\frac{\partial^2\psi}{\partial\phi^2} = \omega + 2\epsilon h^4v,\tag{2.7}$$

where  $\omega = \mathbf{h} \cdot \mathbf{\omega} = h^2 \zeta$ . Here, the quantities  $\psi, \omega, v$  are related to the streamfunction, the helical vorticity and the helical velocity, respectively.

Taking the density  $\rho$  to be constant, the incompressible Euler and vorticity equations become

$$\frac{\partial \boldsymbol{u}}{\partial t} + \boldsymbol{\omega} \times \boldsymbol{u} = -\boldsymbol{\nabla} \left( \frac{p}{\rho} + \frac{1}{2} |\boldsymbol{u}|^2 \right), \tag{2.8}$$

$$\frac{\partial \boldsymbol{\omega}}{\partial t} + \boldsymbol{\nabla} \times (\boldsymbol{\omega} \times \boldsymbol{u}) = 0. \tag{2.9}$$

The above equations could be generalized to a barotropic fluid with pressure a function of density. In helical components, the nonlinear evolution equations for v and  $\omega$  become

$$\frac{\mathrm{D}v}{\mathrm{D}t} = \frac{\partial v}{\partial t} + J(\psi, v) = 0, \tag{2.10}$$

$$\frac{\mathrm{D}\omega}{\mathrm{D}t} = \frac{\partial\omega}{\partial t} + J(\psi, \omega) = 2\epsilon h^4 \left( J(\psi, v) - \epsilon v \frac{\partial v}{\partial \phi} \right),\tag{2.11}$$

where J(f,g) is the Jacobian in helical coordinates:

$$J(f,g) = \frac{1}{r} \left( \frac{\partial \psi}{\partial r} \frac{\partial v}{\partial \phi} - \frac{\partial \psi}{\partial \phi} \frac{\partial v}{\partial r} \right). \tag{2.12}$$

It is clear that the quantity v is materially conserved. In the special case when v is piecewise constant,  $\omega$  is also materially conserved except where v has a discontinuity.

### 3. INVERTING $\mathcal{L}\psi$

Given the relation (2.7) between  $\omega$  and the helical streamfunction  $\psi$ , we now need to invert the operator  $\mathcal{L}\psi$ . Then to compute the velocity field, we differentiate  $\psi$  with respect to r and  $\psi$  and use (2.6). [20] gave a method for the inversion by decomposing  $\psi$  and  $\omega$  as a Fourier series in  $\phi$  and using Green's functions for each mode. In this section, we use a similar approach, but start with a direct Green's function solution that is suitable for a contour dynamics approach.

We write the Green's function solution to (2.7) as

$$\psi = \int G(r, \phi_0; r_0, \phi_0) F(r_0, \phi_0) J_0 dr_0 d\phi_0.$$
(3.1)

where  $F(r,\phi) = \omega + 2\epsilon h^4 v$  and the area element in helical coordinates is  $J_0 dr_0 dh_0$  with  $J_0 = r_0 h(r_0) = r_0 h_0$ . The Green's function  $G(r,\phi_0;r_0,\phi_0)$  satisfies

$$\mathcal{L}G(r,\phi_0;r_0,\phi_0) = \delta(x - x_0) = J_0^{-1}\delta(r - r_0)\delta(\phi - \phi_0). \tag{3.2}$$

Using a Fourier series in the helical variable  $\phi$  leads to a decomposition of G in the form

$$G(r, r_0; \phi, \phi_0) = \sum_m \hat{G}_m(r; r_0) e^{im(\phi - \phi_0)}.$$
 (3.3)

Then (2.7) and (3.2) lead to the ordinary differential equations

$$h\left[\frac{\mathrm{d}}{\mathrm{d}r}\left(rh^{2}\frac{\mathrm{d}}{\mathrm{d}r}\right) - \frac{m^{2}}{r}\right]\hat{G}_{m} = h\left[\frac{r}{1 + \epsilon^{2}r^{2}}G''_{m} + \frac{1 - \epsilon^{2}r^{2}}{(1 + \epsilon^{2}r^{2})^{2}}G'_{m} - \frac{m^{2}}{r}G_{m}\right] = \frac{\delta(r - r_{0})}{2\pi}.$$
 (3.4)

With  $\hat{G}_m$  bounded at origin and infinity, it can be shown that, for  $m \neq 0$ ,  $\hat{G}_m$  takes the form

$$\hat{G}_m(r;r_0) = A_0 \begin{cases} rI'_m(\epsilon m r)K'_m(\epsilon m r_0) & r < r_0, \\ rK'_m(\epsilon m r)I'_m(\epsilon m r_0) & r > r_0, \end{cases}$$

$$(3.5)$$

where  $A_0$  is a function of  $r_0$ , and  $I_m$  and  $K_m$  are the modified Bessel functions of the first and second kind of order m. Primes denote derivatives with respect to r. The jump condition at  $r = r_0$  in (3.4) can be solved to give  $A_0 = \epsilon^2 r_0/(2\pi h_0)$ . We can now rewrite (3.5) as

$$\hat{G}_{m}(r;r_{0}) = \frac{\epsilon^{2} r r_{0}}{2\pi h_{0}} \begin{cases} I'_{m}(\epsilon m r) K'_{m}(\epsilon m r_{0}) & r < r_{0}, \\ K'_{m}(\epsilon m r) I'_{m}(\epsilon m r_{0}) & r > r_{0}. \end{cases}$$
(3.6)

For the axisymmetric mode with m = 0, (3.4) becomes

$$h\left[\frac{\mathrm{d}}{\mathrm{d}r}(rh^2\hat{G}_0')\right] = \frac{\delta(r-r_0)}{2\pi},\tag{3.7}$$

which we can solve directly to give

$$\hat{G}_0(r; r_0) = \begin{cases} 0 & r < r_0, \\ \frac{1}{2\pi h_0} \int_{r_0}^r \frac{\mathrm{d}r_1}{r_1 h^2(r_1)} & r > r_0. \end{cases}$$
(3.8)

Note that  $\hat{G}_0$  does not decay at infinity, although its derivative does.

#### 4. CONTOUR DYNAMICS

We take the boundary of the vortex to be given by f = 0 where f is a scalar function with f > 0 inside the vortex. By assuming that v is piecewise constant, we can take the solutions of (2.10) and (2.11) in the form

$$\omega = BH[f] + \Omega |\nabla f| \delta[f], \qquad v = CH[f] + v_{\infty}. \tag{4.1}$$

In (4.1), B gives the helical component of vorticity inside the vortex and C gives the helical velocity increment inside the vortex compared to the helical velocity component in the far field.

The function  $\Omega$ , which evolves in time, is the strength of the vortex sheet. The presence of the vortex sheet is signaled by the form of (2.11): vorticity is generated when the right-hand side is nonzero. For piecewise continuous  $\omega$  and v, this only happens on the boundary, giving a vortex sheet. Other situations when this happens are, for example, in the presence of jumps in density and swirl, as discussed in [18]. The functions H and  $\delta$  are the Heaviside and delta functions, respectively. With this form, the field f is materially conserved, so that

$$\frac{\mathrm{D}f}{\mathrm{D}t} = 0. \tag{4.2}$$

We require the velocity field to decay in the far field. Appendix A shows that helical symmetry leads to the constraint

$$v_{\infty} = -\left[\frac{\epsilon}{2\pi} \oint_{\mathcal{S}} \frac{B}{h} dS + \frac{\epsilon^2 C}{\pi} \oint_{\mathcal{S}} h^3 dS + \frac{\epsilon}{2\pi} \oint_{\mathcal{C}} \gamma d\xi\right], \tag{4.3}$$

where  $\oint_{\mathcal{S}}$  denotes the surface integral over the vortex,  $\oint_{\mathcal{C}}$  is the contour integral along the vortex boundary and  $\gamma \equiv \Omega L/h$ . The variable  $\xi$  is a parameter taken clockwise along the vortex boundary in the  $(r, \phi)$  plane, and L is defined in (A.5). For the special case when C and  $\Omega$  vanish, we find

$$v_{\infty} = -\frac{\epsilon}{2\pi} \oint_{S} \frac{B}{h} \, \mathrm{d}S. \tag{4.4}$$

From (2.11) and (4.1), the vortex sheet strength is governed by

$$\frac{\mathrm{D}\Omega}{\mathrm{D}t}|\nabla f| + \Omega \frac{\mathrm{D}|\nabla f|}{\mathrm{D}t} = 2\epsilon h^4 \left[ CJ(\psi, f) - \frac{1}{2}\epsilon (C^2 + 2Cv_\infty) \frac{\partial f}{\partial \phi} \right]. \tag{4.5}$$

The factor of 1/2 comes from the product of H and  $\delta$ .

Let  $(r, \phi) = (R(\xi, t), \Phi(\xi, t))$  be a parametric representation of the boundary. Then the Lagrangian advection equations for the contour  $(R, \Phi)$  in helical coordinates are

$$\frac{\partial R}{\partial t} = u_r(R, \Phi, t), \qquad \frac{\partial \Phi}{\partial t} = \frac{1}{Rh(R)} u_\phi(R, \Phi, t),$$
 (4.6)

where  $\partial/\partial t$  is the Lagrangian derivative taken at constant  $\xi$ . A representation of the contour is shown in Fig. 2.

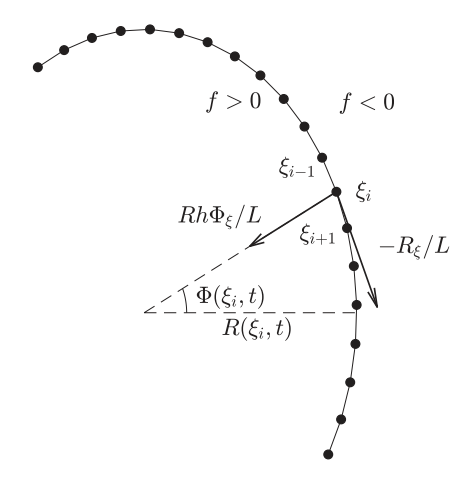


Fig. 2. Schematic of the contour  $(R(\xi,t),\Phi(\xi,t))$  with f>0 on the inside and f<0 outside of the patch. The parameterization  $\xi$  is taken clockwise along the patch boundary, and the dots represent the corresponding spatial discretization.

Following the approach of [16], we find (details are given in Appendix B)

$$\frac{1}{|\nabla f|} \frac{D|\nabla f|}{Dt} = \frac{1}{L} \frac{\partial L}{\partial t} + \epsilon^2 h^2 R u_r, \tag{4.7}$$

with  $L(\xi,t)$  defined in (A.5). Consider  $\Omega$  as a function of  $\xi$  and t; then (4.5) can be written as

$$\frac{\partial \Omega}{\partial t} + \Omega \left( \frac{1}{L} \frac{\partial L}{\partial t} + \epsilon^2 h^2 R \frac{\partial R}{\partial t} \right) = \frac{2\epsilon h^4}{L} \left[ C \left( -\frac{\partial R}{\partial \xi} u_\phi + Rh \frac{\partial \Phi}{\partial \xi} u_r \right) + \frac{1}{2} \epsilon (C^2 + 2Cv_\infty) Rh \frac{\partial R}{\partial \xi} \right]. \tag{4.8}$$

By introducing  $\gamma = \Omega L/h$ , (4.8) can be simplified to

$$\frac{\partial \gamma}{\partial t} = 2\epsilon h^3 \left[ C \left( -\frac{\partial R}{\partial \xi} u_\phi + Rh \frac{\partial \Phi}{\partial \xi} u_r \right) + \frac{1}{2} \epsilon (C^2 + 2Cv_\infty) Rh \frac{\partial R}{\partial \xi} \right]. \tag{4.9}$$

When v is uniform and there is no vortex sheet on the boundary initially, we have  $C = \gamma(0) = 0$ . Then there will be no vortex sheet generated at later times. It is useful to examine the limits of this result as  $\epsilon$  becomes small or large. In the  $\epsilon \to 0$  limit, the right-hand side vanishes, so there is no Lagrangian evolution of the vortex sheet, as expected. As  $\epsilon \to \infty$ ,  $\omega = \mathbf{h} \cdot \mathbf{\omega} = -(\epsilon r)^{-1} \mathbf{e}_{\theta} \cdot \mathbf{\omega}$ , so that  $\Omega \sim -\epsilon^{-1}\Omega_{HM}$ . Similarly,  $v = h^{-2}\mathbf{h} \cdot \mathbf{u} = -\epsilon r \mathbf{e}_{\theta} \cdot \mathbf{u}$ , and  $C \sim -\epsilon C_{HM}$ . As  $L \sim L_{HM}$  in this limit, (4.8) recovers the result (2.23) of [15].

The approach of [6] can now be applied to obtain a contour dynamics formulation. The stream function  $\psi$  can be decomposed into two parts,  $\psi_S$  and  $\psi_H$ , which are obtained from the vortex sheet and vortex patch, respectively. In (3.1), the vortex sheet contribution  $F_s = \Omega |\nabla f| \delta(f)$  leads, using (A.2), to the following contour integrals for  $\psi_S$ :

$$\frac{\partial \psi_S}{\partial r} = \oint_{\mathcal{C}} \frac{\partial G}{\partial r} \Omega(\xi) L(\xi) \, \mathrm{d}\xi, \qquad \frac{\partial \psi_S}{\partial \phi} = \oint_{\mathcal{C}} \frac{\partial G}{\partial \phi} \Omega(\xi) L(\xi) \, \mathrm{d}\xi. \tag{4.10}$$

To obtain the rest of the velocity field, we start with Green's theorem (A.1) in the variables  $r_0$  and  $\phi_0$ . Defining new functions by

$$rh\frac{\partial P}{\partial \phi_0} = r_0 h_0 \frac{\partial G}{\partial \phi}, \qquad \frac{1}{r_0 h_0} \frac{\partial (r_0 h_0 Q)}{\partial r_0} = \frac{1}{r_0 h_0^5} \frac{\partial (r_0 h_0 S)}{\partial r_0} = \frac{\partial G}{\partial r},$$
 (4.11)

we find

$$P(r,\phi;r_0,\phi_0) = -\frac{r_0 h_0}{rh} \sum_{m \neq 0} \hat{G}_m(r;r_0) e^{im(\phi - \phi_0)}, \tag{4.12}$$

$$Q(r,\phi;r_0,\phi_0) = \frac{1}{r_0 h_0} \sum_{m} \int_{-\infty}^{\infty} \frac{\partial \hat{G}_m(r;r_1)}{\partial r} r_1 h_1 \, dr_1 e^{im(\phi - \phi_0)}, \tag{4.13}$$

$$S(r,\phi;r_0,\phi_0) = \frac{1}{r_0 h_0} \sum_{r=1}^{r} \int_{-\infty}^{\infty} \frac{\partial \hat{G}_m(r;r_1)}{\partial r} r_1 h_1^5 \, \mathrm{d}r_1 e^{\mathrm{i}m(\phi-\phi_0)}. \tag{4.14}$$

There is freedom in the definition of P since its m = 0 component is not specified. From (3.1), one arrives at the equations

$$\frac{\partial \psi_H}{\partial r} = \oint_{\mathcal{S}} \frac{\partial G}{\partial r} (B + 2\epsilon C h_0^4) r_0 h_0 \, dr_0 \, d\phi_0 + 2\epsilon v_\infty \int_{\mathbb{R}^2} \frac{\partial G}{\partial r} r_0 h_0^5 \, dr_0 \, d\phi_0$$

$$= B \oint_{\mathcal{C}} Q r_0 h_0 \, d\phi_0 + 2\epsilon C \oint_{\mathcal{C}} S r_0 h_0 \, d\phi_0 + \epsilon v_\infty r, \qquad (4.15)$$

$$\frac{\partial \psi_H}{\partial \phi} = \oint_{\mathcal{S}} \frac{\partial G}{\partial \phi} (B + 2\epsilon h_0^4 C) r_0 h_0 \, dr_0 \, d\phi_0 + 2\epsilon v_\infty \int_{\mathbb{R}^2} \frac{\partial G}{\partial \phi} r_0 h_0^5 \, dr_0 \, d\phi_0$$

$$= -rh \oint_{\mathcal{C}} P(B + 2\epsilon h_0^4 C) \, dr_0. \qquad (4.16)$$

Then from (2.6) the corresponding velocity components can be obtained as

$$u_r(r,\phi,t) = -\frac{1}{r} \left( \frac{\partial \psi_S}{\partial \phi} + \frac{\partial \psi_H}{\partial \phi} \right), \qquad u_\phi(r,\phi,t) = h \left( \frac{\partial \psi_S}{\partial r} + \frac{\partial \psi_H}{\partial r} \right). \tag{4.17}$$

Together (4.6), (4.9), (4.10) and (4.15)–(4.17) form a closed set of equations governing the motion of the boundary.

### 5. STABILITY ANALYSIS

In this section we perform a linear stability analysis for a circular vortex patch with radius  $R_0$ . The perturbed boundary is  $r = R_0 + \eta(\phi, t)$ . We consider the general case and compare the results in the absence of a vortex sheet to those of [20].

### 5.1. Base Flow

We start from a basic state that is a function of r alone. We take the quantities v and  $\omega$  to be piecewise constant inside, taking values  $V_0$ ,  $Q_0$  and  $V_{\infty}$ , 0 inside and outside the patch, while  $\Omega_0$  is constant along the patch boundary. (This corresponds to  $Q = Q_0$  and  $C = V_0 - V_{\infty}$ .) Then (2.7) can be written as

$$\mathcal{L}\Psi_1 = \frac{1}{r} \frac{\mathrm{d}}{\mathrm{d}r} \left( rh^2 \frac{\mathrm{d}\Psi_1}{\mathrm{d}r} \right) = Q_0 + 2\epsilon h^4 V_0, \quad 0 < r < R_0, \tag{5.1}$$

$$\mathcal{L}\Psi_2 = \frac{1}{r} \frac{\mathrm{d}}{\mathrm{d}r} \left( rh^2 \frac{\mathrm{d}\Psi_2}{\mathrm{d}r} \right) = 2\epsilon h^4 V_{\infty}, \quad r > R_0, \tag{5.2}$$

which can be solved directly to give

$$\frac{d\Psi_1}{dr} = \frac{Q_0 r}{2} (1 + \epsilon^2 r^2) + V_0 \epsilon r, \quad 0 < r < R_0$$
 (5.3)

$$\frac{\mathrm{d}\Psi_2}{\mathrm{d}r} = \frac{c}{r}(1 + \epsilon^2 r^2) + V_\infty \epsilon r, \quad r > R_0 \tag{5.4}$$

with  $d\Psi_1/dr$  bounded at the origin. There is no axial velocity at infinity, so that

$$\lim_{r \to \infty} u_z = \lim_{r \to \infty} h^2 \left( V_{\infty} + \epsilon r \frac{\mathrm{d}\Psi_2}{\mathrm{d}r} \right) = \lim_{r \to \infty} (V_{\infty} + \epsilon c) = 0.$$
 (5.5)

This leads to

$$\frac{\mathrm{d}\Psi_2}{\mathrm{d}r} = -\frac{V_\infty}{\epsilon r}, \quad r > R_0. \tag{5.6}$$

In this case,  $u_z = 0$  identically outside the vortex patch. From (4.3), or alternatively working out the jump in  $d\Psi/dr$  directly from  $R_0h_0^2[d\Psi/dr]_0 = R_0\Omega$  with  $h_0 = h(R_0)$ , we find the constraint

$$\Omega = -\frac{Q_0 R_0}{2} - h_0^2 \left( V_0 \epsilon R_0 + \frac{V_\infty}{\epsilon R_0} \right). \tag{5.7}$$

When there is no vortex sheet on the boundary and the along-helix velocity increment is zero, i. e.,  $\Omega_0 = C = 0$ , one finds continuity of  $u_\theta$  and  $u_z$  across the boundary at  $r = R_0$ .

### 5.2. Perturbation Equations

Denote perturbations with primes. Then from (2.7), (2.10) and (2.11), the linearized perturbed equations are

$$\frac{1}{r}\frac{\partial}{\partial r}\left(rh^2\frac{\partial\psi'}{\partial r}\right) + \frac{1}{r}\frac{\partial^2\psi'}{\partial\phi^2} = 0,\tag{5.8}$$

$$\frac{\partial v'}{\partial t} + \frac{1}{r} \frac{\mathrm{d}\Psi}{\mathrm{d}r} \frac{\partial v'}{\partial \phi} = 0, \tag{5.9}$$

$$\frac{\partial \omega'}{\partial t} + \frac{1}{r} \frac{\mathrm{d}\Psi}{\mathrm{d}r} \frac{\partial \omega'}{\partial \phi} = 0. \tag{5.10}$$

In these equations,  $\psi'$  represents both  $\psi'_1$  and  $\psi'_2$  and so on.

Consider the boundary of the patch described by  $f = R_0 + \eta(\phi, t) - r$ . From the kinematic boundary condition (4.2), we can write

$$0 = \frac{\partial \eta}{\partial t} + \frac{1}{r} \frac{\partial \psi}{\partial r} \frac{\partial \eta}{\partial \phi} + \frac{1}{r} \frac{\partial \psi}{\partial \phi}$$
 (5.11)

at  $r = R_0 + \eta$ , valid both inside and outside the patch. On linearization, the kinetic boundary conditions become

$$0 = \frac{\partial \eta}{\partial t} + \frac{1}{r} \frac{\mathrm{d}\Psi_1}{\mathrm{d}r} \frac{\partial \eta}{\partial \phi} + \frac{1}{r} \frac{\partial \psi_1'}{\partial \phi} = \frac{\partial \eta}{\partial t} + \frac{1}{r} \frac{\mathrm{d}\Psi_2}{\mathrm{d}r} \frac{\partial \eta}{\partial \phi} + \frac{1}{r} \frac{\partial \psi_2'}{\partial \phi}$$
(5.12)

at  $r = R_0$ .

For the dynamic boundary condition, we start with the momentum equation in the  $\phi$ -direction

$$\frac{\partial u_{\phi}}{\partial t} + u_{r} \frac{\partial u_{\phi}}{\partial r} + \frac{u_{\phi}}{rh} \frac{\partial u_{\phi}}{\partial \phi} + \frac{u_{\phi}u_{r}}{r} = -\frac{1}{\rho rh} \frac{\partial p}{\partial \phi}.$$
 (5.13)

Substituting from (2.6) leads to

$$h\frac{\partial^2 \psi}{\partial t \partial r} - \frac{1}{r} \frac{\partial \psi}{\partial \phi} \frac{\partial}{\partial r} \left( h \frac{\partial \psi}{\partial r} \right) + \frac{h}{r} \frac{\partial \psi}{\partial r} \frac{\partial^2 \psi}{\partial \phi \partial r} - \frac{h}{r^2} \frac{\partial \psi}{\partial \phi} \frac{\partial \psi}{\partial r} = -\frac{1}{\rho r h} \frac{\partial p}{\partial \phi}. \tag{5.14}$$

Since the pressure is continuous across the boundary, so is  $\partial p/\partial \phi$ . Then, at the boundary  $r = R_0$ , we obtain the linearized dynamic boundary condition

$$h\frac{\partial^{2}\psi_{1}'}{\partial t\partial r} - \frac{1}{r}\frac{\partial\psi_{1}'}{\partial \phi}\frac{\partial}{\partial r}\left(h\frac{\mathrm{d}\Psi_{1}}{\mathrm{d}r}\right) + \frac{h}{r}\frac{\mathrm{d}\Psi_{1}}{\mathrm{d}r}\frac{\partial^{2}\psi_{1}'}{\partial \phi\partial r} - \frac{h}{r^{2}}\frac{\partial\psi_{1}'}{\partial \phi}\frac{\mathrm{d}\Psi_{1}}{\mathrm{d}r}$$

$$=h\frac{\partial^{2}\psi_{2}'}{\partial t\partial r} - \frac{1}{r}\frac{\partial\psi_{2}'}{\partial \phi}\frac{\partial}{\partial r}\left(h\frac{\mathrm{d}\Psi_{2}}{\mathrm{d}r}\right) + \frac{h}{r}\frac{\mathrm{d}\Psi_{2}}{\mathrm{d}r}\frac{\partial^{2}\psi_{2}'}{\partial \phi\partial r} - \frac{h}{r^{2}}\frac{\partial\psi_{2}'}{\partial \phi}\frac{\mathrm{d}\Psi_{2}}{\mathrm{d}r}.$$
(5.15)

# 5.3. Dispersion Relation

Introduce the normal modes with  $[\omega', \psi'_1, \psi'_2, \eta] = [\hat{\omega}(r), \hat{\psi}_1(r), \hat{\psi}_2(r), \hat{\eta}]e^{st+im\phi}$ , where m is a nonnegative integer. Starting with (5.8) for the perturbed helical stream function leads to the following ordinary differential equations:

$$\frac{1}{r}\frac{\mathrm{d}}{\mathrm{d}r}\left(rh^2\frac{\mathrm{d}\hat{\psi}}{\mathrm{d}r}\right) - \frac{m^2}{r}\hat{\psi} = 0,\tag{5.16}$$

corresponding to the homogeneous version of (3.4). Hence,  $\hat{\psi}$  takes the same form as the complementary functions used to construct (3.5). For  $\hat{\psi}_1$  and  $\hat{\psi}_2$  to be bounded at r=0 and  $\infty$ , we require

$$\hat{\psi}_1 = B_1 r I_m'(\epsilon m r), \qquad \hat{\psi}_2 = B_2 r K_m'(\epsilon m r), \tag{5.17}$$

where  $B_1$  and  $B_2$  are constants and m > 0. The two boundary conditions (5.12) and (5.15) then lead to

$$B_2 K'_m(\alpha) \left( s + \frac{\mathrm{i}m}{R_0} \frac{\mathrm{d}\Psi_1}{\mathrm{d}r} \right) = B_1 I'_m(\alpha) \left( s + \frac{\mathrm{i}m}{R_0} \frac{\mathrm{d}\Psi_2}{\mathrm{d}r} \right), \tag{5.18}$$

$$B_1\left[\left(sh + \frac{\mathrm{i}mh}{R_0}\frac{\mathrm{d}\Psi_1}{\mathrm{d}r}\right)I - \mathrm{i}mI_m'F_1\right] = B_2\left[\left(sh + \frac{\mathrm{i}mh}{R_0}\frac{\mathrm{d}\Psi_2}{\mathrm{d}r}\right)K - \mathrm{i}mK_m'F_2\right],\tag{5.19}$$

with all functions evaluated at  $R_0$ . Here we write  $F_{1,2} = h\left(h^2\Psi'_{1,2}/R_0 + \Psi''_{1,2}\right)$ ,  $I = I'_m + \alpha I''_m$  and  $K = K'_m + \alpha K''_m$  with  $\alpha = \epsilon m R_0$ . We also write  $I'_m = I'_m(\alpha)$  and so on. Multiplying (5.18) by (5.19) leads to the quadratic dispersion relation

$$-\frac{s^{2}}{\epsilon^{2}R_{0}^{2}h} + s\frac{\mathrm{i}m}{R_{0}} \left[ K'_{m} \left( 2h\frac{\mathrm{d}\Psi_{1}}{\mathrm{d}r}I - R_{0}I'_{m}F_{1} \right) - I'_{m} \left( 2h\frac{\mathrm{d}\Psi_{2}}{\mathrm{d}r}K - R_{0}K'_{m}F_{2} \right) \right] - \frac{m^{2}}{R_{0}^{2}} \left[ K'_{m} \frac{\mathrm{d}\Psi_{1}}{\mathrm{d}r} \left( h\frac{\mathrm{d}\Psi_{1}}{\mathrm{d}r}I - R_{0}I'_{m}F_{1} \right) - I'_{m} \frac{\mathrm{d}\Psi_{2}}{\mathrm{d}r} \left( h\frac{\mathrm{d}\Psi_{2}}{\mathrm{d}r}K - R_{0}K'_{m}F_{2} \right) \right] = 0.$$
 (5.20)

The growth rates in this general case are hence given by the roots of the quadratic  $as^2 + bs + c = 0$ . As is typical for inviscid Hamiltonian systems, the growth rates are either imaginary or complex with opposite real parts. The roots s will have positive real part if

$$\Delta = K_m'^2 I_m'^2 (F_1 - F_2)^2 + \frac{4h^2}{R_0^2} h_1 h_2 \left( \Psi_1' - \Psi_2' \right)^2 + \frac{4h}{R_0} K_m' I_m' (h_1 F_2 - h_2 F_1) (\Psi_1' - \Psi_2') < 0, \quad (5.21)$$

with  $h_1 = h * I * K'_m$  and  $h_2 = h * K * I'_m$ . Figure 3 shows the resulting stability region for different wavenumbers, m, and nondimensionalized radius,  $\epsilon R_0$ . It can be observed for all cases that a larger wavenumber corresponds to a smaller stability region.

When the velocities are continuous across the boundary, i. e.,  $\Psi'_1 = \Psi'_2$  at r = R, the dispersion relation reduces to the linear equation

$$s = -\mathrm{i} m Q_0 \left( \frac{1}{2} + \epsilon^2 R_0^2 K_m'(\alpha) I_m'(\alpha) \right). \tag{5.22}$$

The linear frequencies  $\Omega_m$  (nondimensionalized appropriately) are

$$\Omega_m = -\frac{\mathrm{i}s}{mQ_0} = -\left(\frac{1}{2} + \epsilon^2 R_0^2 K_m'(\alpha) I_m'(\alpha)\right). \tag{5.23}$$

This is the same result as [20]. For  $\alpha \ll 1$ , it tends to the two-dimensional value  $(m^{-1}-1)/2$ ; for  $\alpha \gg 1$ , it tends to the axisymmetric values  $\epsilon R_0/2m$  [1]. These results indicate that Re(s)=0 for a pure circular helical vortex patch, which is hence linearly neutrally stable. However, nonlinear evolution may lead to instability. Here we have only discussed vortex patches centered at origin. Unlike the 2D case, there is no simple basic state for an off-center vortex patch.

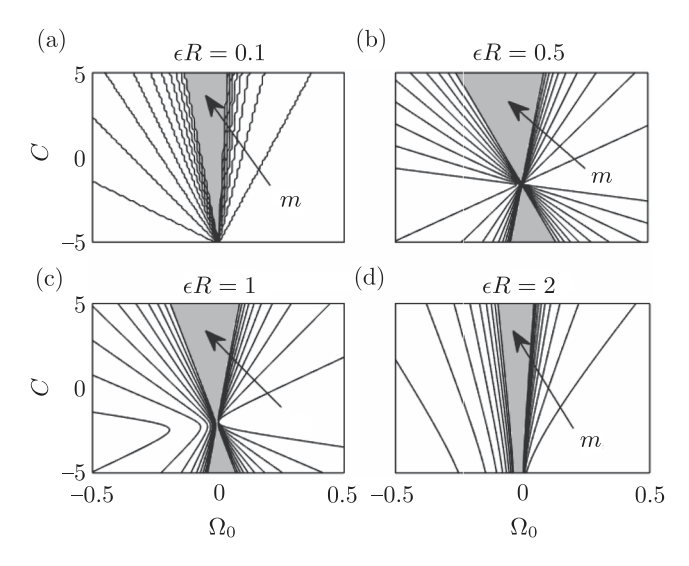


Fig. 3. Stability regions of different radial wavenumbers  $m=1,2,\cdots,10$  for (a)  $\epsilon R_0=0.1$ ; (b)  $\epsilon R_0=0.5$ ; (c)  $\epsilon R_0=1$ ; (d)  $\epsilon R_0=2$ . The stability regions are the wedge-shaped regions (shaded region) encompassing  $\Omega=0$  pointed to by the arrows.

### 6. CONTOUR DYNAMICS CALCULATIONS

We now use the contour dynamics method described above to examine the stability of circular vortex patches. The parameter space is extensive, as C and  $\Omega_0$  can be varied, along with  $\epsilon R_0$ . Our goal is to illustrate the method, so we consider only a few cases. An examination of the full parametric dependence is left for another time.

We place N = 128 nodes on the boundary to represent the contour. Following the approach of [3], we use Fourier series in terms of the parameter  $\xi$  to interpolate between these nodes using

$$R(\xi) = \operatorname{Re} \left\{ \sum_{k=-N/2}^{N/2-1} \hat{R}_k e^{ik\xi} \right\}, \qquad \Phi(\xi) = \operatorname{Re} \left\{ \sum_{k=-N/2}^{N/2-1} \hat{\Phi}_k e^{ik\xi} \right\}, \tag{6.1}$$

where  $\hat{R}_k$  and  $\hat{\Phi}_k$  are the Fourier transform of R and  $\Phi$ , and  $\xi$  is equally spaced in  $[0,2\pi)$ . The terms  $\partial R/\partial \xi$  and  $\partial \Phi/\partial \xi$  can be obtained directly by differentiating (6.1) with respect to  $\xi$ . For a given mode m, the corresponding initial Fourier coefficient is set as  $\hat{\eta}_m(0)$ . The simulations are performed with  $R_0 = 1$ ,  $\epsilon = 1$  and  $Q_0 = 1$ . The quantity  $v_\infty$  is obtained from the constraint in (4.4). The initial strength of the vortex sheet,  $\Omega_0$ , is set to be zero for the first three simulations. For the ith node, we obtain  $\partial R_i/\partial t$  and  $\partial \Phi_i/\partial t$  from (4.6) and (4.16)–(4.17), and  $\partial \gamma_i/\partial t$  from (4.9). The contour integrals are computed using the trapezoidal rule, then R,  $\Phi$  and  $\gamma$  are advanced in time using a fourth-order Runge–Kutta method with time step  $\delta t = 0.0125$ . The integrals in (4.13), (4.14) are calculated with a lower limit 0.0001 to avoid the singularities of modified Bessel functions of the second kind at the origin.

# 6.1. No Along-helix Velocity Jump

We first consider the case that there is no jump in the along-helix velocity, i. e., C=0. No vortex sheet is generated in the evolution, as discussed in Section 4. Figure 4 shows the time evolution of vortex patch in the  $r-\phi$  plane with initial perturbation  $\hat{\eta}_4(0) = 10^{-3}$ . The counterclockwise rotation of the contour is due to the basic state. The contour remains circular in the evolution, so the linear stability of the patch, as given in Section 5.3, appears to be robust.

We examine the evolution of the normal mode coefficient shown in Fig. 5. Results for the analytic solution obtained from (5.23) are shown for comparison. The numerical solution follows the linear solution well initially, but starts to drift as time progresses.

The constraint (4.3) is required by the helical symmetry. In the computation, however, this constraint is only enforced initially. During the time span plotted in Figs. 4–5, the relative error in  $v_{\infty}$  is  $10^{-4}$  (not shown), which gives an estimate of the numerical error.

### 6.2. Jumps in Along-helix Velocity

We now consider a positive velocity jump, C=1, which doubles the basic state angular velocity at the edge of the vortex. A vortex sheet is generated when the initial circular patch is perturbed. Figure 3 shows that this basic state is linearly stable. Figure 6 shows the evolution of the perturbed circular contour. Again the vortex stays circular. Figure 7 displays the evolution of the coefficient of mode 4. Again the linear solution is followed by a gradual departure.

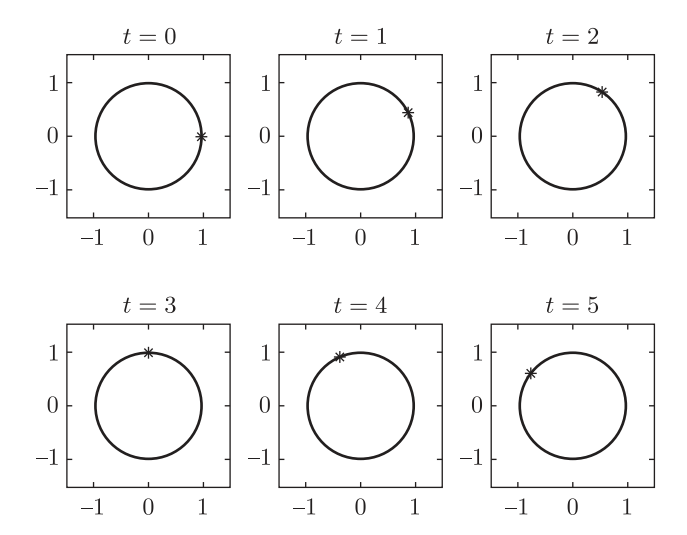


Fig. 4. Contour evolution in the  $r-\phi$  plane with initial perturbation  $\hat{\eta}_4(0) = 10^{-3}$  and velocity jump C = 0. The star denotes a reference node of the discretization.

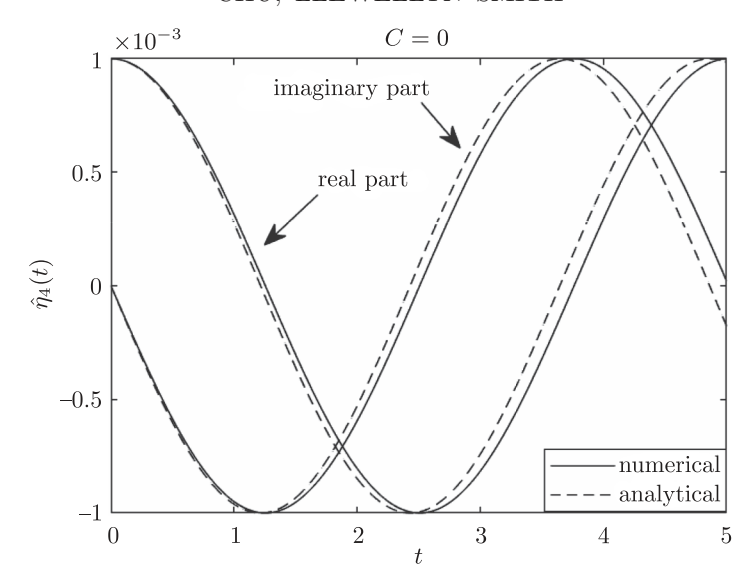


Fig. 5. Time evolution of  $\hat{\eta}_4(t)$  with velocity jump C=0: (a) real part; (b) imaginary part. The analytic solution is obtained using the linear angular frequency  $\Omega_4=-0.3230$  from (5.23).

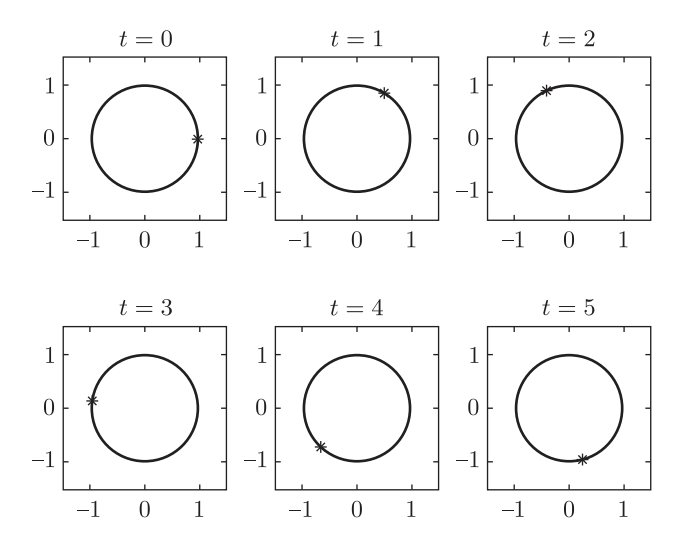


Fig. 6. Contour evolution in the  $r-\phi$  plane with initial perturbation  $\hat{\eta}_4(0) = 10^{-3}$  and velocity jump C = 1. The star denotes a reference node of the discretization.

The strength of the vortex sheet is given by  $\gamma = \Omega L/h$ . Figure 8 shows the distribution of  $\gamma$  along the normalized boundary length at different instants for the case with velocity jump C=1. Here, the first node of the discretization corresponds to  $\tilde{l}=0$  and  $\tilde{l}=1$  coincides with  $\tilde{l}=0$ . Note that the same value of  $\tilde{l}$  does not generally correspond to the same fluid particle for different instants since the distance between successive nodes changes with time. It can be seen that the distribution of  $\gamma$  is smooth and sinusoidal, dominated by mode 4.

We also consider the case with a negative jump, C = -1, when the basic state is at rest outside the vortex and on its boundary. The vortex patch starts evolving when a perturbation is imposed to the circular contour, which leads to the generation of the vortex sheet, see (4.9). Figure 9 shows the corresponding contour evolution. The contour remains circular, and the reference node does not move. The evolution of the mode amplitude and vortex sheet density is similar to the case C = 1.

#### 6.3. Initial Vortex Sheet

We now consider the case when a uniform vortex sheet is present in the basic state. The initial vortex sheet strength,  $\Omega_0$ , is 0.2, which corresponds to a linearly unstable vortex. When C = 0, the

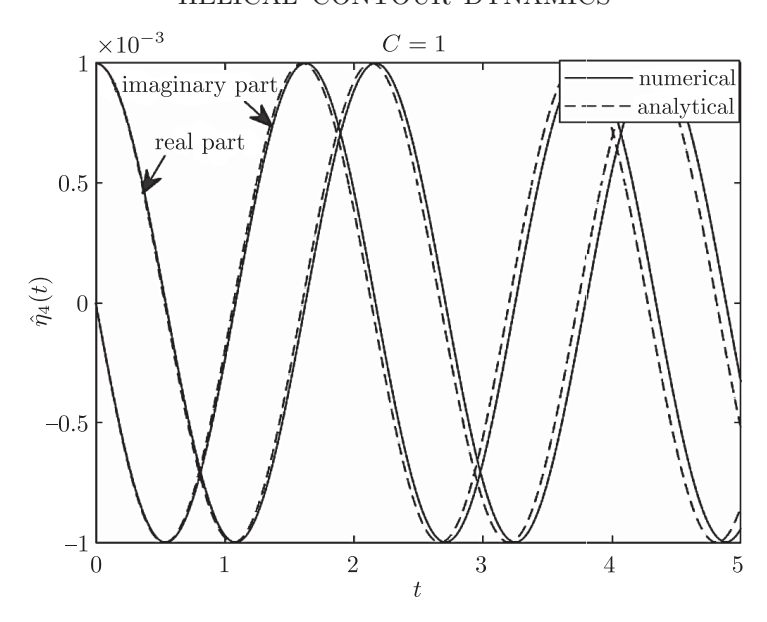


Fig. 7. Time evolution of  $\hat{\eta}_4(t)$  with velocity jump C=1: (a) real part; (b) imaginary part. The analytic solution is obtained using the linear angular frequency  $\Omega_4=-0.7346$  from (5.20).

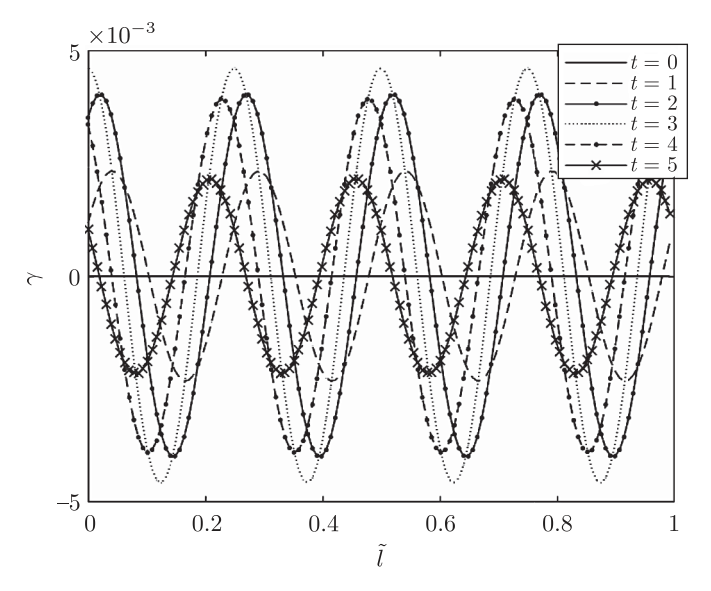


Fig. 8. Vortex sheet strength,  $\gamma = \Omega L/h$ , along the normalized boundary length,  $\tilde{l}$ , at different instants for the case with with velocity jump C = 1.

strength of the vortex sheet stays the same from (4.9). Figure 10 shows the corresponding contour evolution for the case with  $\Omega_0 = 0.2$  and C = 0. The dominant linear mode 4 is clearly growing. For small times, its behavior is shown in Fig. 11 and matches the linear prediction well, but for times greater than 2 or so the evolution starts to differ as nonlinear effects become important.

Finally, we consider the case when a uniform vortex sheet and a positive jump in along-helix velocity are both present in the basic state. In this case the strength of the vortex sheet evolves in time. Figure 12 displays the evolution of the coefficient of mode 4 when  $\Omega_0 = 0.05$ . The numerical solution follows the stable linear solution with a gradual departure. Some numerical noise is observed at the peaks and valleys of the trajectory, but overall the evolution is smooth.

Figure 13 shows the distribution of  $\gamma$  along the normalized boundary length at different instants for this case. Compared to the case shown in Fig. 8, it can be seen that the distribution of  $\gamma$  is shifted from its initial value as time progresses.

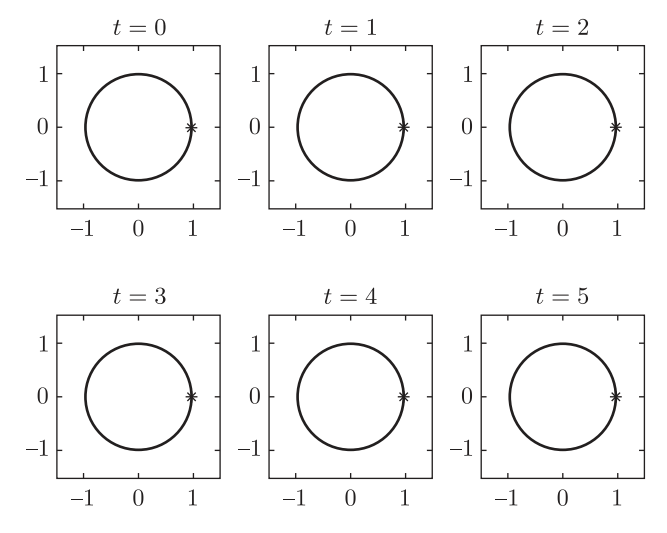


Fig. 9. Contour evolution in the r- $\phi$  plane with initial perturbation  $\hat{\eta}_4(0) = 10^{-3}$  and velocity jump C = -1. The star denotes a reference node of the discretization.

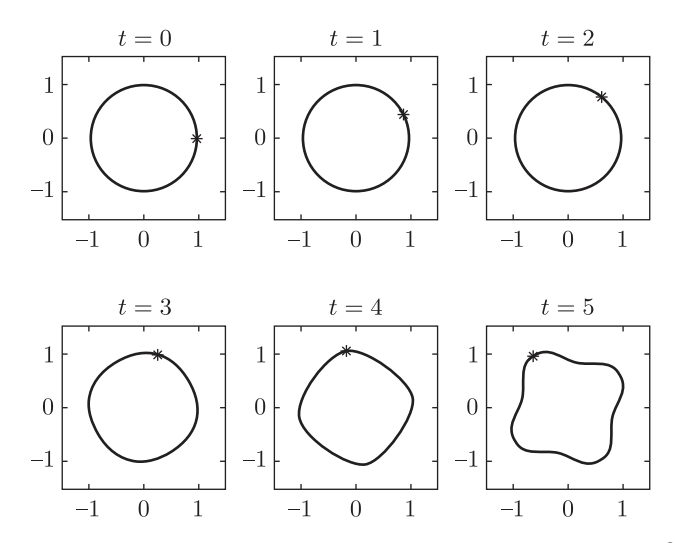


Fig. 10. Contour evolution in the  $r-\phi$  plane with initial perturbation  $\hat{\eta}_4(0) = 10^{-3}$ , vortex sheet strength  $\Omega_0 = 0.2$  and no helix-along velocity jump. The star denotes a reference node of the discretization.

### 7. CONCLUSIONS

In this work we have described contour dynamics for helically symmetric flows. We use a direct Green's function solutions for different Fourier modes and express the streamfunction using contour integrals using Green's theorem in helical coordinates. The CD algorithm includes the compatibility condition (4.3), an evolution equation for the vorticity-like variable  $\gamma$  (gamma), and integrals along the contour to compute the velocity components needed (4.15)–(4.16).

We use the phrase "contour dynamics" to refer to Lagrangian algorithms that track boundary motion, in which velocities and other quantities can be computed using integrals along contours. This is the case for the work of [25, 35, 37] in which no vortex sheet is generated, but has been used to describe subsequent investigations which included further physics [3, 15, 16, 19]. With this nomenclature, the Birkhoff–Rott equation also corresponds to a CD algorithm, but it is older and has its own name. This is also true for algorithms for vortex sheets with density differences. The standard review article on contour dynamics of Pullin [26] mentions the helical case, without giving any details, so our appellation follows precedent. The current paper is the first to work out the details.

Two limiting cases,  $\epsilon \to 0$  and  $\epsilon \to \infty$ , recover the two-dimensional and axisymmetric results, respectively. The Lagrangian evolution of the contour boundary is obtained by considering the

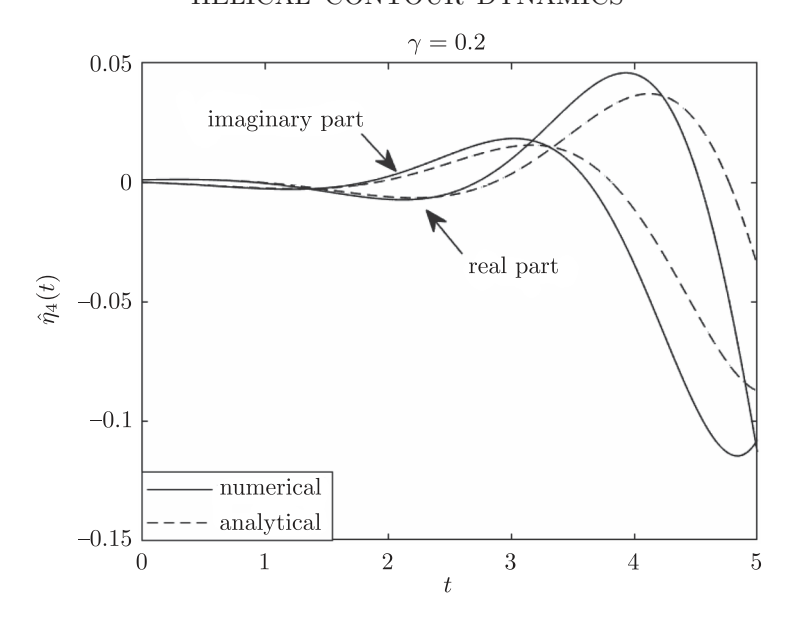


Fig. 11. Time evolution of  $\hat{\eta}_4(t)$  with initial vortex sheet  $\Omega_0 = 0.2$  and no helix-along velocity jump: (a) real part; (b) imaginary part. The analytic solution is obtained using the growth rate  $s_4 = 0.9091 - 1.6466i$  from (5.20).

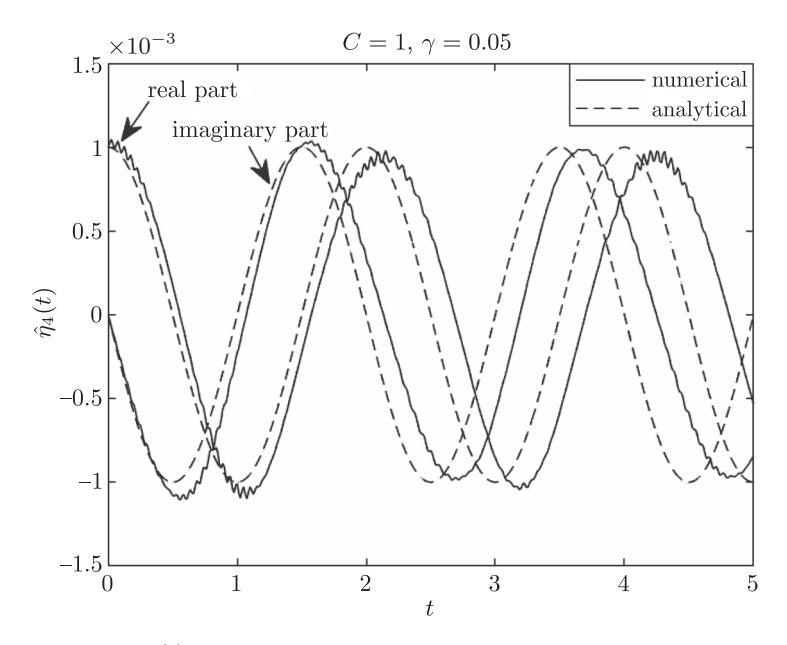


Fig. 12. Time evolution of  $\hat{\eta}_4(t)$  with velocity jump C=1 and initial vortex sheet  $\Omega_0=0.05$ : (a) real part; (b) imaginary part. The analytic solution is obtained using the linear angular frequency  $\Omega_4=-0.7855$  from (5.20).

contributions from the vortex sheet and the vortex patch. This contour dynamics system is interesting as it has two evolving variables for a purely hydrodynamic system. We have carried out a linear stability analysis for a circular vortex patch with helical symmetry including both a vortex sheet and a velocity jump in the helical direction. While the velocity jump may seem analogous to Kelvin–Helmholtz instability, the constraints of helical symmetry strongly affect it, and in particular the presence of a velocity jump does not always lead to instability and ill-posedness with unbounded growth rates for large wavenumbers. The latter result is not surprising as there is now a length scale in the problem, namely,  $\epsilon^{-1}$ .

We demonstrate the use of the contour dynamics approach by examining the evolution of a perturbed circular patch numerically. Previous work considered the case with continuous v, in

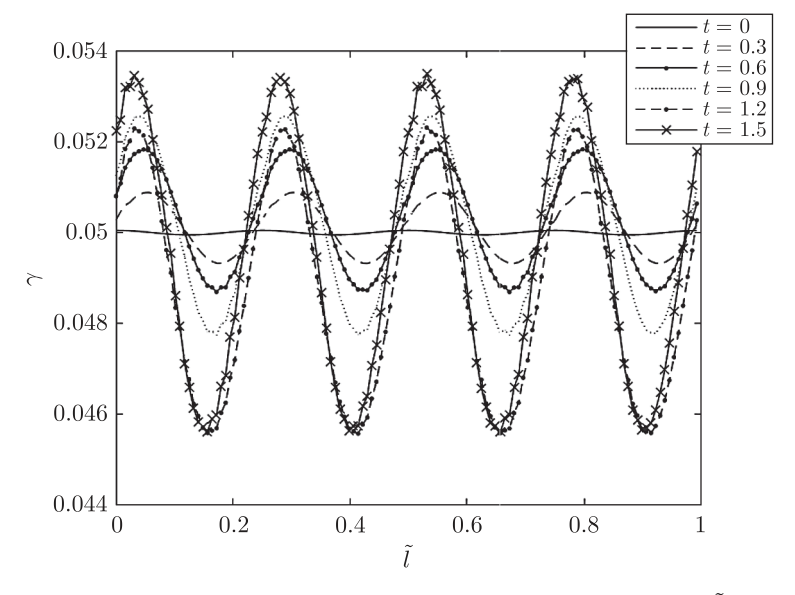


Fig. 13. Vortex sheet strength,  $\gamma = \Omega L/h$ , along the normalized boundary length,  $\tilde{l}$ , at different instants for the case with velocity jump C = 1 and initial vortex sheet  $\Omega_0 = 0.05$ .

which case the patch is neutrally stable. Here we examine the full problem and obtain regions of linear stability, as shown in Fig. 3. The results agree well with the linear solution for small time, but for the unstable cases considered, the nonlinear and linear evolution starts to diverge. These calculations use the full formulation of the CD algorithm, with  $\gamma$  evolving in time. The effects of the interplay between along-helix velocity and vortex sheet evolution are intriguing and merit quantification.

# APPENDIX A. DERIVATION OF (4.3)

We write Green's theorem in the plane in the form

$$\oint_{\mathcal{S}} \left( \frac{1}{rh} \frac{\partial (rhQ)}{\partial r} - \frac{1}{rh} \frac{\partial P}{\partial \phi} \right) rh \, dr \, d\phi = \oint_{\mathcal{C}} (P \, dr + rhQ \, d\phi). \tag{A.1}$$

We also use the result

$$\oint_{\mathcal{S}} A\delta(f) |\nabla f| \, \mathrm{d}S = \int_{C} AL \, \mathrm{d}\xi, \tag{A.2}$$

where  $dS = rh dr d\phi$  and the zero contour of the function f defines the contour C. This equation reduces to the expected results in the two-dimensional and axisymmetric limits.

For an arbitrary contour, consider the integral

$$\Gamma = \oint_{\mathcal{S}} (\omega + 2\epsilon h_0^4 v) r dr d\phi = \oint [u_r dr + r h u_\phi d\phi], \tag{A.3}$$

where the last equality has been obtained using (A.1). Evaluating the integral over a large circle of radius R and using (4.1), we find

$$\Gamma = B \oint_{\mathcal{S}} r \, dr \, d\phi + \int_{\mathcal{C}} \frac{\Omega L}{h} \, d\xi + 2\epsilon C \oint_{\mathcal{S}} h^4 r \, dr \, d\phi + 2\epsilon v_{\infty} \int_{\mathcal{S}_R} h^4 r \, dr \, d\phi, \tag{A.4}$$

where S and C are the surface and boundary of the vortex. The metric term L is defined on a curve  $(R(\xi), \Phi(x))$  by

$$L^{2}(\xi,t) = \left(Rh\frac{\partial\Phi}{\partial\xi}\right)^{2} + \left(\frac{\partial R}{\partial\xi}\right)^{2}.$$
 (A.5)

The final term in (A.4) can be computed exactly and has the limit  $2\pi v_{\infty}\epsilon^{-1}$  as  $R\to\infty$ . For large r, the nonzero Fourier modes of  $\psi$  decay rapidly, so that

$$\frac{\partial \psi}{\partial r} \sim -\frac{v_{\infty}}{\epsilon r} + \frac{D}{r} (1 + \epsilon^2 r^2),$$
 (A.6)

while, from (A.3),  $\Gamma \sim 2\pi D$ . Substituting the forms for  $u_r$  and  $u_z$  into (2.5) shows that, for  $u_z$  to decay at large r, we must have  $D = \Gamma = 0$ . Using this result in (A.4) leads to (4.3). The resulting constraint comes from the fact that zero flow at infinity when the flow at infinity is helical implies that the circulation vanishes, and does not apply to two-dimensional or axisymmetric flow.

# APPENDIX B. DERIVATION OF (4.7)

The contour f is materially conserved, so that (4.2) leads to

$$0 = \nabla f \cdot \nabla \frac{\mathrm{D}f}{\mathrm{D}t} = |\nabla f| \cdot \frac{\partial |\nabla f|}{\partial t} + |\nabla f|(\mathbf{u} \cdot \nabla)|\nabla f| + \nabla f \cdot [(\nabla f \cdot \nabla)\mathbf{u}]. \tag{B.1}$$

Hence, we obtain

$$\frac{1}{|\nabla f|} \frac{D|\nabla f|}{Dt} = -\mathbf{n} \cdot [(\mathbf{n} \cdot \nabla)\mathbf{u}], \tag{B.2}$$

where  $\mathbf{n} = \nabla f/|\nabla f| = n_r \mathbf{e}_r + n_\phi \mathbf{e}_\phi$  is a unit vector normal to the contour f = 0. Then

$$-\mathbf{n} \cdot \left[ (\mathbf{n} \cdot \nabla) \mathbf{u} \right] = -n_r \left( u_r \frac{\partial u_r}{\partial r} + \frac{u_\phi}{rh} \frac{\partial u_r}{\partial \phi} - \frac{u_\phi h}{r} u_\theta \right) - n_\phi h \left( u_r \frac{\partial u_\theta}{\partial r} + \frac{u_\phi}{rh} \frac{\partial u_\theta}{\partial \phi} + \frac{u_\phi h}{r} u_r \right) - n_\phi \epsilon h r \left( u_r \frac{\partial u_z}{\partial r} + \frac{u_\phi}{rh} \frac{\partial u_z}{\partial \phi} \right). \tag{B.3}$$

Relating the tangent to the normal vector using

$$\frac{1}{L}\frac{\partial R}{\partial \xi} = -n_{\phi}, \qquad \frac{Rh}{L}\frac{\partial \Phi}{\partial \xi} = n_{r}, \tag{B.4}$$

and using (A.5), we find

$$-\frac{1}{L}\frac{\mathrm{D}L}{\mathrm{D}t} = n_{\phi}\left(-n_{\phi}\frac{\partial u_{r}}{\partial r} + \frac{n_{r}}{Rh}\frac{\partial u_{r}}{\partial \phi}\right) - n_{r}\left(n_{r}\frac{h^{2}}{R}u_{r} - n_{\phi}\frac{\partial u_{\phi}}{\partial r} + \frac{n_{r}}{Rh}\frac{\partial u_{\phi}}{\partial \phi} + n_{\phi}\frac{h^{2}}{R}u_{\phi}\right). \tag{B.5}$$

Combining the continuity equation

$$\nabla \cdot \mathbf{u} = \frac{\partial u_r}{\partial r} + \frac{u_r}{r} + \frac{1}{rh} \frac{\partial u_\phi}{\partial \phi} = 0$$
 (B.6)

with (B.3) and (B.5) yields

$$\frac{1}{|\nabla f|} \frac{D|\nabla f|}{Dt} = \frac{1}{L} \frac{DL}{Dt} + \epsilon^2 h^2 R u_r.$$
(B.7)

The  $\epsilon \to 0$  and  $\epsilon \to \infty$  recover the two-dimensional and axisymmetric results, respectively.

The left-hand side of (4.5) can hence be written as

$$\Omega_t + \Omega \frac{L_t}{L} + \Omega \epsilon h^2 R R_t = \Omega_t + \Omega \frac{L_t}{L} - \Omega \frac{h_t}{h}, \tag{B.8}$$

where we are now using  $\partial_t$  to designate Lagrangian derivatives since quantities are defined on the vortex boundary and where we have used the result  $h_t = -\epsilon^2 R h^3 R_t$ . This leads to (4.7).

# FUNDING

Part of this research was supported by NSF Award CBET-1706934.

REGULAR AND CHAOTIC DYNAMICS Vol. 26 No. 6 2021

### CONFLICT OF INTEREST

The authors declare that they have no conflicts of interest.

### REFERENCES

- Saffman, P. G., Vortex Dynamics, Cambridge Monogr. Mech. Appl. Math., New York: Cambridge Univ. Press, 1992.
- 2. Alekseenko, S. V., Kuibin, P. A., Okulov, V. L., and Shtork, S. I., Helical Vortices in Swirl Flow, J. Fluid Mech., 1999, vol. 382, pp. 195–243.
- 3. Chang, Ch., Llewellyn Smith, S. G., Axisymmetric Contour Dynamics for Buoyant Vortex Rings, J. Fluid Mech., 2020, vol. 887, A28, 28 pp.
- 4. Delbende, I., Rossi, M., and Piton, B., Direct Numerical Simulation of Helical Vortices, Int. J. Eng. Syst. Model. Simul., 2012, vol. 4, nos. 1–2, pp. 94–101.
- 5. Delbende, I., Piton, B., and Rossi, M., Merging of Two Helical Vortices, Eur. J. Mech. B Fluids, 2015, vol. 49, part B, pp. 363–372.
- 6. Dritschel, D. G., Contour Dynamics and Contour Surgery: Numerical Algorithms for Extended High-Resolution Modelling of Vortex Dynamics in Two-Dimensional, Inviscid, Incompressible Flows, *Comput. Phys. Rep.*, 1989, vol. 10, no. 3, pp. 77–146.
- 7. Dritschel, D.G., Generalized Helical Beltrami Flows in Hydrodynamics and Magnetohydrodynamics, J. Fluid Mech., 1991, vol. 222, pp. 525–541.
- 8. Felli, M., Camussi, R., and Di Felice, F., Mechanisms of Evolution of the Propeller Wake in the Transition and Far Fields, *J. Fluid Mech.*, 2011, vol. 682, pp. 5–53.
- 9. Fukumoto, Y. and Okulov, V. L., The Velocity Field Induced by a Helical Vortex Tube, *Phys. Fluids*, 2005, vol. 17, no. 10, 107101, 19 pp.
- Gupta, B.P. and Loewy, R.G., Theoretical Analysis of the Aerodynamic Stability of Multiple, Interdigitated Helical Vortices, AIAA J., 1974, vol. 12, no. 10, pp. 1381–1387.
- 11. Hattori, Y. and Fukumoto, Y., Short-Wavelength Stability Analysis of a Helical Vortex Tube, *Phys. Fluids*, 2009, vol. 21, no. 1, 014104, 7 pp.
- 12. Hattori, Y. and Fukumoto, Y., Short-Wave Stability of a Helical Vortex Tube: The Effect of Torsion on the Curvature Instability, *Theor. Comput. Fluid Dyn.*, 2010, vol. 24, nos. 1–4, pp. 363–368.
- 13. Hattori, Y. and Fukumoto, Y., Effects of Axial Flow on the Stability of a Helical Vortex Tube, *Phys. Fluids*, 2012, vol. 24, no. 5, 054102, 15 pp.
- 14. Hattori, Y. and Fukumoto, Y., Modal Stability Analysis of a Helical Vortex Tube with Axial Flow, J. Fluid Mech., 2014, vol. 738, pp. 222–249.
- 15. Hattori, Y. and Llewellyn Smith, S. G., Motion of Axisymmetric Magnetic Eddies with Swirl, *Procedia IUTAM*, 2013, vol. 7, pp. 243–250.
- Hattori, Y. and Moffatt, H. K., Evolution of Toroidal Magnetic Eddies in an Ideal Fluid, J. Fluid Mech., 2006, vol. 558, pp. 253–279.
- 17. Kuibin, P. A. and Okulov, V. L., Self-Induced Motion and Asymptotic Expansion of the Velocity Field in the Vicinity of a Helical Vortex Filament, *Phys. Fluids*, 1998, vol. 10, no. 3, pp. 607–614.
- 18. Llewellyn Smith, S. G., Chang, C., Chu, T., Blyth, M., Hattori, Y., and Salman, H., Generalized Contour Dynamics: A Review, *Regul. Chaotic Dyn.*, 2018, vol. 23, no. 5, pp. 507–518.
- 19. Llewellyn Smith, S. G. and Hattori, Y., Axisymmetric Magnetic Vortices with Swirl, *Commun. Nonlinear Sci. Numer. Simul.*, 2012, vol. 17, no. 5, pp. 2101–2107.
- 20. Lucas, D. and Dritschel, D. G., A Family of Helically Symmetric Vortex Equilibria, J. Fluid Mech., 2009, vol. 634, pp. 245–268.
- 21. Okulov, V., On the Stability of Multiple Helical Vortices, J. Fluid Mech., 2004, vol. 521, pp. 319–342.
- 22. Okulov, V. L. and Sørensen, J. N., Stability of Helical Tip Vortices in Rotor Far Wake, *J. Fluid. Mech.*, 2007, vol. 576, pp. 1–25.
- 23. Okulov, V. and Sørensen, J. N., The Self-Induced Motion of a Helical Vortex, J. FLuid Mech., 2020, vol. 883, A5, 19 pp.
- 24. Okulov, V. L., Sørensen, J. N., and Wood, D. H., The Rotor Theories by Professor Joukowsky: Vortex Theories, *Prog. Aerosp. Sci.*, 2015, vol. 73, pp. 19–46.
- 25. Pozrikidis, C., The Nonlinear Instability of Hill's Vortex, J. Fluid Mech., 1986, vol. 168, pp. 337–367.
- 26. Pullin, D. I., Contour Dynamics Methods, Annu. Rev. Fluid Mech., 1992, vol. 24, pp. 89–115.
- 27. Ricca, R. L., The Effect of Torsion on the Motion of a Helical Vortex Filament, J. Fluid Mech., 1994, vol. 273, pp. 241–259.
- 28. Riley, N., The Fascination of Vortex Rings, Appl. Sci. Res., 1997, vol. 58, nos. 1–4, pp. 169–189.
- 29. Selçuk, C., Delbende, I., and Rossi, M., Helical Vortices: Quasiequilibrium States and Their Time Evolution, *Phys. Rev. Fluids*, 2017, vol. 2, no. 8, 084701, 27 pp.
- 30. Sherry, M., Nemes, A., Lo Jacono, D., Blackburn, H. M., and Sheridan, J., The Interaction of Helical Tip and Root Vortices in a Wind Turbine Wake, *Phys. Fluids*, 2013, vol. 25, 117102, 16 pp.

- 31. Shariff, K., Leonard, A., and Ferziger, J.H., A Contour Dynamics Algorithm for Axisymmetric Flow, J. Comp. Phys., 2008, vol. 227, no. 21, pp. 9044–9062.
- 32. Velasco Fuentes, O., Motion of a Helical Vortex, J. Fluid Mech., 2018, vol. 836, R1, 11 pp.
- 33. Durán Venegas, E. and Le Dizès, S., Generalized Helical Vortex Pairs, J. Fluid Mech., 2019, vol. 865,
- pp. 523–545. 34. Widnall, S. E., The Stability of a Helical Vortex Filament, *J. Fluid Mech.*, 1972, vol. 54, no. 4, pp. 641–
- 35. Zabusky, N. J., Hughes, M. H., and Roberts, K. V., Contour Dynamics for the Euler Equations in Two Dimensions, J. Comp. Phys., 1979, vol. 30, no. 1, pp. 96–106.
- 36. Delbende, I. and Rossi, M., Dynamics of the Three Helical Vortex System and Instability, in *Internat*. Conf. on Aerodynamics of Offshore Wind Energy Systems and Wakes (ICOWES, Lyngby, June 2013),  $12 \,\mathrm{pp}$ .
- 37. Shariff, K., Leonard, A., and Ferziger, J., Dynamics of a Class of Vortex Rings, NASA Tech. Memo. No. 102257 (1989).